https://doi.org/10.1016/j.jmst.2021.01.054

Machine Learning of Phases and Mechanical Properties in Complex Concentrated Alloys

Jie XIONG[b,c], San-Qiang SHI[b,c]*, Tong-Yi ZHANG[a,d]*

[a] School of Materials Science and Engineering, Harbin Institute of Technology, Shenzhen, China

[b]Department of Mechanical Engineering, The Hong Kong Polytechnic University, Hong Kong, China

[c]Shenzhen Research Institute, The Hong Kong Polytechnic University, Shenzhen, China

[d]Material Genome Institute, Shanghai University, Shanghai, China

Abstract

The mechanical properties of complex concentrated alloys (CCAs) depend on their formed phases and corresponding microstructures. The data-driven prediction of the phase formation and associated mechanical properties is essential to discovering novel CCAs. The present work collects 557 samples of various chemical compositions, comprising 61 amorphous, 167 single-phase crystalline, and 329 multi-phases crystalline CCAs. Three classification models are developed with high accuracies to category and understand the formed phases of CCAs. Also, two regression models are constructed to predict the hardness and ultimate tensile strength of CCAs, and the correlation coefficient of the random forest regression model is greater than 0.9 for both of two targeted properties. Furthermore, the Shapley additive explanation (SHAP) values are calculated, and accordingly four most important features are identified. A significant finding in the SHAP values is that there exists a critical value in each of the top four features, which provides an easy and fast assessment in the design of improved mechanical properties of CCAs. The present work demonstrates the great potential of machine learning in the design of advanced CCAs.

Keywords

Materials Informatics, SHAP, Complex Concentrated Alloys, High Entropy Alloys

1. Introduction

The conventional alloys contain only one principal element in each alloy, which is usually called the principal element based alloy. The mechanical properties of a principal element based alloy are generally predominated by the principal element[1]. In contrast, complex concentrated alloys (CCAs) are composed of multiple principal elements with more or less same percentage and have excellent mechanical properties and unexpected micro-structures. The multiple principal elements render high configuration entropy if the CCAs in solid solution, thereby called high-entropy alloys. Actually, CCAs encompass medium-entropy alloys (MEAs) consisting of three or four principal components and high-entropy alloys (HEAs) consisting of more than four principal components[2–7].

According to the Gibbs phase rule $F = C - P + 1$ (where F is the degree of freedom, C is the number of components and P is the number of phases), multiple elements might produce ($C + 1$) equilibrium phases in CCAs, a maximum of six equilibrium phases are expected in the case of a five-component CCA[8]. However, the high configuration entropy in a CCA can enhance the formation of a single phase rather than multiple phases[3,9]. Thus, some CCAs were reported to form single-phase disordered solid solutions with simple body-centered-cubic (BCC)[10], face-centered-cubic (FCC)[11], or hexagonal close-packed (HCP)[12] lattice structure, and some CCAs were found to form single intermetallic phase, such as C14 Laves phase[13] and B2 phase[14]. Multiple disordered solid-solutions[15] and multiple intermetallic phases[16] are termed here as multi-phase CCAs. Besides, some amorphous CCAs have been developed in the past decades[17]. Therefore, in the present work, a CCA belongs to one of three crystalline sets of amorphous (AM), single-phase (SP), and multi-phases (MP).

Figure 1 shows that the mechanical properties of CCAs depend on their formed phases; the MP CCAs are stronger than the SP CCAs, the CCAs that contain intermetallic phases (termed as IM) are stronger than the CCAs that only consists of solid solutions (termed as SS), the SP-BCC and MP-BCC CCAs are harder and stronger than the SP-FCC and MP-FCC CCAs. In materials computation, researchers conduct thermodynamic modeling, density functional theory (DFT) calculations, and molecular dynamics (MD) simulation in order to design CCAs from elements. For example, Gorsse et al.[18] applied the CALPHAD method to predict the phase formation of CCAs, Huhn et al.[19] utilized the DFT approach to predict the phase

transformation in CCAs. The large number of elements in CCAs, however, gives rise to the difficulty and cost of those computation techniques. Recently, the materials community employs Machine learning (ML) to investigate and design novel materials, including steels[20–22], metallic glasses[23–27], shape memory alloys[28], and CCAs[29–31]. For instance, Wen et al.[29] proposed a ML-based strategy to find new CCAs with high hardness in the Al-Co-Cr-Cu-Fe-Ni system. Islam et al.[30] employed a neural network to classify the corresponding phase selection in 118 CCAs with an average test accuracy of higher than 80%. Huang et al.[31] adopted and compared three different ML algorithms on 401 CCAs to predict the crystalline phases. The distinction between single-phase and multi-phases and the formation of HCP solid solutions, however, have not been considered yet in ML of CCAs. The hardness of only one specific CCA system has been studied by ML [29], although big hardness data are available in the literature for many CCA systems. The yield strength of CCAs has been investigated by the ML approach [32], whereas the ultimate tensile strength of CCAs has not been investigated by ML at all.

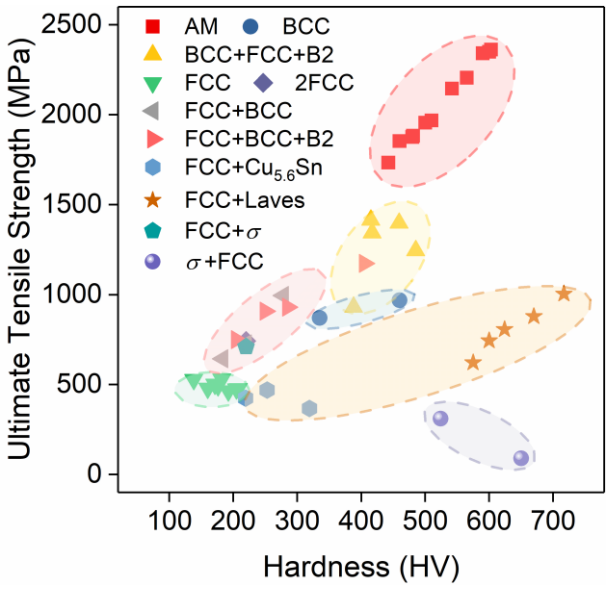

Figure 1. Ashby plot of ultimate tensile strength versus hardness of CCAs with different crystalline phases, where the first phase in each label of multi-phases is the matrix, e.g., BCC is the matrix for BCC+FCC+B2.

In this work, we proposed a ML framework to investigate the phase formation ability and predict the mechanical properties of CCAs. A dataset of CCAs was constructed by collecting data from related studies. These data covered variables such as processing conditions, resulting phases, hardness, and ultimate tensile strength (UTS). A large number of features were initially introduced, and various feature selection algorithms were utilized to select key features during

model construction. A random forest classifier (RFC) was used to classify the formed phases in CCAs, while a random forest regressor (RFR) was employed to predict the hardness and UTS of CCAs.

2. Methodology

2.1 Data Acquisition

In addition to chemical compositions, the fabrication conditions of CCAs play an essential role in the phase formation of CCAs. Therefore, only the fabrication by vacuum arc melting-cast is considered here, and 750 as-cast CCAs are collected from five review articles [33–37] and several related studies [37-54]. There have been some samples with conflict reports on phases in the 750 as-cast CCAs; excluding the conflict data reduces the data number to 557. The present phase dataset includes 61 AM samples, 136 SP-SS samples, 31 SP-IM samples, 94 MP-SS samples, and 235 MP-IM samples. The RFC is conducted on all 557 data, called ML-A dataset, to classify AM, SP, and MP. The number of crystalline-set, termed ML-B dataset, is 496, on which RFC will classify SS and IM. The 230 SS CCAs form ML-C dataset, with which RFC classify HCP sub-cluster, BCC sub-cluster including SP and MP BCC CCAs, FCC sub-cluster including SP and MP FCC CCAs, and mixture (MSS) sub-cluster including the mixture of BCC, FCC, and HCP. Some of the 750 CCAs have reported hardness values, and a few of them have reported UTS values. If the reported values of hardness (or UTS) of a CCA are different, the average value of hardness (or UTS) is adopted for that CCA. The hardness dataset and the UTS dataset in the present study consist of 290 and 71 CCAs, respectively. All the collected data are listed in Tables S1-S3 in the Supplementary Material.

2.2 Feature Construction

Table 1 lists feature blocks, including 22 elemental parameters, 5 thermodynamic parameters, and 3 valence electron distributions. The elemental properties of a CCA can be approximately estimated by the atomic average value $\bar{x}$ as,

$$\bar{x} = \sum_{i=1}^{n} a_i x_i \quad (1)$$

where a_i and x_i is the atomic fraction and elemental properties of the ith element, respectively.

In addition, the mismatch in elemental properties (δ_x) of constituent elements is also employed to describe each CCA, which is defined by

$$\delta_x = \sqrt{\sum a_i \left(1 - {}^{x_i}/_{\bar{x}}\right)^2} \tag{2}$$

The five thermodynamic parameters are the enthalpy of mixing (H_{mix}) [56], the entropy of mixing (S_{mix}) [56], the entropy of fusion ($S_f = \overline{H_f}/\overline{T_m}$) with $\overline{H_f}$ and $\overline{T_m}$ being average heat of fusion and average melting temperature, respectively [57], Gibbs free energy of mixing (G_{mix}) [58], and the $1/\Omega = |H_{\mathrm{mix}}|/\overline{T_m}S_{\mathrm{mix}}$ parameter [12, 56] The valence electron distributions comprise the fraction (f_k) of the average electrons in the *s*, *p*, *d* valence orbitals, i.e.,

$$f_k = {}^{\overline{k\mathrm{VEC}}}/_{\overline{\mathrm{VEC}}} \quad (k = s, p, d \text{ orbitals}) \tag{3}$$

where the overbar means the average obtained by Equation 1. In this way, 30 features are initially generated with the feature blocks and then normalized to [0, 1] according to:

$$x' = \frac{x - \min x}{\max x - \min x} \tag{4}$$

where *x'* is the normalized feature, min *x* and max *x* are the minimum and maximum values of the original feature *x*, respectively.

2.3 Evaluation Metrics

The performances of classification are evaluated by the miss rate and accuracy, which are defined by

$$Miss\ Rate = \frac{F}{T + F} \tag{5}$$

$$Accuracy = 1 - Miss\ Rate = \frac{T}{T + F} \tag{6}$$

where *T* and *F* stand for the number of correctly and wrongly classified samples, respectively.

The performances of regression models are evaluated by the normalized root mean squared error (*NRMSE*) and correlation coefficient (*r*):

$$NRMSE = \frac{\sqrt{\sum_{i=1}^{n} \frac{1}{n} (\hat{y}_i - y_i)^2}}{\bar{y}} \tag{7}$$

$$r = \sqrt{\frac{\sum_{i=1}^{n} (\hat{y}_i - \bar{y})^2}{\sum_{i=1}^{n} (y_i - \bar{y})^2}} \tag{8}$$

y_i and $\hat{y}_i$ is the actual and corresponding predicted value, and $\bar{y}$ is the mean of actual values.

The value of $r = 1$ indicates perfect fitting.

Table 1. Feature blocks consisting of elemental parameters, thermodynamic parameters, and VEC distributions.

	Description	*Abb.*	Definition
Elemental parameters	Atomic Number	*AN*	$\bar{x} = \sum a_i x_i$ $\delta_x = \sqrt{\sum a_i (1 - {x_i}/{\bar{x}})^2}$
	Metallic Radius	*MR*	
	Melting Point	*Tm*	
	Boiling Point	*Tb*	
	Pauling Electronegativity	*XP*	
	Electron Affinity	*Eea*	
	First Ionization Potential	*I*1	
	Molar Heat Capacity	*Cm*	
	Thermal Conductivity	*K*	
	Valence Electron	VEC	
	Heat of Fusion	*Hf*	
Thermodynamic parameters	Enthalpy of mixing	H_{mix}	$H_{\mathrm{mix}} = 4\sum_{i=1}^{N}\sum_{j=1}^{N}\Delta H_{ij} a_i a_j$
	Entropy of mixing	S_{mix}	$S_{\mathrm{mix}} = -R\sum_{i=1}^{N} a_i \ln a_i$
	Entropy of fusion	S_f	$S_f = {\overline{H_f}}/{\overline{T_m}}$
	Gibbs free energy of mixing	G_{mix}	$G_{mix} = H_{\mathrm{mix}} - S_{\mathrm{mix}} \cdot \overline{T_m}$
	The reciprocal of Ω	$1/\Omega$	$1/\Omega = {\lvert H_{\mathrm{mix}} \rvert}/{\overline{T_m} S_{\mathrm{mix}}}$
VEC distributions	fraction of the electrons in the *s* valence orbitals	f_s	$f_s = {\overline{s\mathrm{VEC}}}/{\overline{\mathrm{VEC}}}$
	fraction of the electrons in the *p* valence orbitals	f_p	$f_s = {\overline{p\mathrm{VEC}}}/{\overline{\mathrm{VEC}}}$
	fraction of the electrons in the *d* valence orbitals	f_d	$f_s = {\overline{d\mathrm{VEC}}}/{\overline{\mathrm{VEC}}}$

2.4 Validation method

The ten-fold cross-validation method is employed, where each dataset is randomly divided into ten folds, nine folds as the training set and one fold as the validation set. In turn, the ML model

is trained on the training set and tested on the validation set ten times. The average of ten test performances then gives the cross-validation performance.

3. Results and Discussion

3.1 Classification of Phase-formations

A good ML model should provide as good as possible performance with as less as possible number of features to achieve a balance between accuracy and complexity. Thus, feature selection should be conducted to remove redundant features. First, linear-correlated features are removed by using the Pearson correlation coefficient (PCC, ρ),

$$\rho_{(x_1,x_2)} = \frac{cov(x_1, x_2)}{\sigma_{x_1}\sigma_{x_2}} \tag{9}$$

where σ_{x_1} and σ_{x_2} denote the standard deviation of features x_1 and x_2, and cov is the covariance. The absolute value of PCC bigger than 0.9 indicates a strong linear correlation between two features and then only one feature of the correlated pair is selected. After that, sequential backward selection (SBS) wrapped with RFC, sequential forward selection (SFS) wrapped with RFC, and mean decrease impurity (MDI) derived from RFC [59] are conducted to screen further the PCC initially selected features. The three feature selection methods are denoted by SBS+RFC, SFS+RFC, and MDI/RFC accordingly.

Table 2. The PCC selected features

Dataset	PCC selected Features
ML-A	$\overline{AN}, \delta_{AN}, \overline{MR}, \delta_{MR}, \delta_{Tb}, \overline{Tm}, \delta_{Tm}, \overline{Eea}, \delta_{Eea}, \delta_{XP}, \overline{Hf}, \delta_{Hf},$ $\overline{I1}, \delta_{I1}, \overline{Cm}, \delta_{Cm}, \overline{K}, \delta_{K}, \overline{\mathrm{VEC}}, \delta_{\mathrm{VEC}}, f_p, H_{\mathrm{mix}}, S_{\mathrm{mix}}, S_f$
ML-B	$\overline{AN}, \delta_{AN}, \overline{MR}, \delta_{MR}, \delta_{Tb}, \overline{Tm}, \delta_{Tm}, \overline{Eea}, \delta_{Eea}, \overline{XP}, \delta_{XP}, \delta_{Hf},$ $\overline{I1}, \delta_{I1}, \overline{Cm}, \delta_{Cm}, \overline{K}, \delta_{K}, \overline{\mathrm{VEC}}, \delta_{\mathrm{VEC}}, f_p, f_d, H_{\mathrm{mix}}, S_{\mathrm{mix}}, S_f, G_{\mathrm{mix}}$
ML-C	$\overline{AN}, \delta_{AN}, \delta_{MR}, \delta_{Tb}, \overline{Tm}, \delta_{Tm}, \overline{Eea}, \delta_{Eea}, \overline{XP}, \delta_{XP}, \delta_{Hf}, \delta_{I1},$ $\overline{Cm}, \delta_{Cm}, \overline{K}, \delta_{K}, \overline{\mathrm{VEC}}, \delta_{\mathrm{VEC}}, f_p, H_{\mathrm{mix}}, S_{\mathrm{mix}}, S_f, G_{\mathrm{mix}}, 1/\Omega$

Figure 2 shows the PCC map between features in the ML-A dataset with the highlighting of strong correlation features. There are six strong-correlated feature pairs, namely, $\overline{MR} - \overline{XP}$, $\overline{Tb} - \overline{Tm}$, $\overline{\mathrm{VEC}} - f_s$, $\overline{\mathrm{VEC}} - f_d$, $H_{\mathrm{mix}} - G_{mix}$ and $H_{\mathrm{mix}} - 1/\Omega$, from which the four features of $\overline{MR}$, $\overline{Tm}$, $\overline{\mathrm{VEC}}$, and H_{mix} are selected [36,60,61]. Thus, the PCC selects 24 features in the

ML-A dataset, which are listed in Table 2. Similarly, the PCC approach (see supplementary material as Figure S1-S2 for details) screens out 26 and 24 features in the ML-B and ML-C datasets, respectively, which are listed in Table 2 as well.

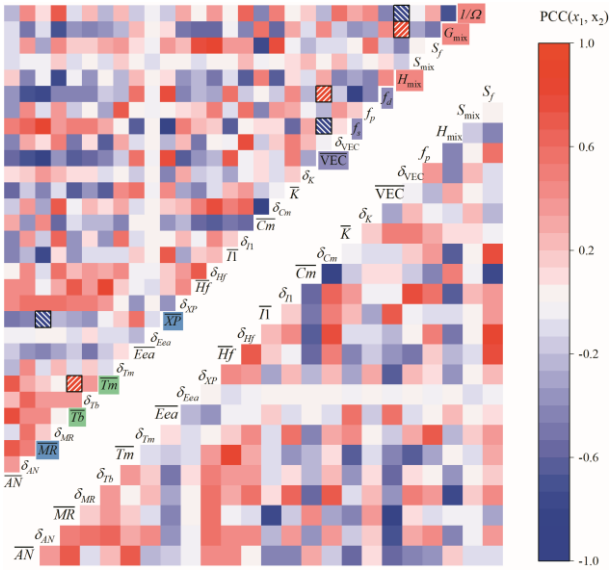

Figure 2. The PCC matrix of features in the ML-A dataset.

The three feature selection methods of SBS+RFC, SFS+RFC, and MDI/RFC are thus conducted to screen further and rank the PCC selected features, and the results are shown in Figures 3(a), 3(b), and 3(c) for the ML-A, ML-B, and ML-C datasets, respectively, where the distance of each feature from the center indicates the feature rank, and the longer the feature distance, the higher the feature rank will be. The features are then ranked by integers sequentially, with one representing the most important feature.

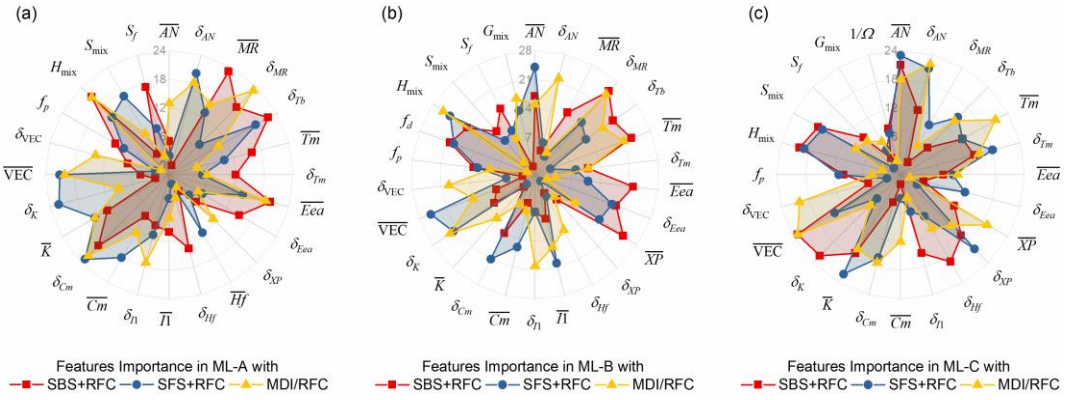

Figure 3. The rank of features in the (a) ML-A, (b) ML-B, and (c) ML-C dataset resulting from on the SBS+RFC (in red), SFS+RFC (in blue), and MDI/RFC (in yellow).

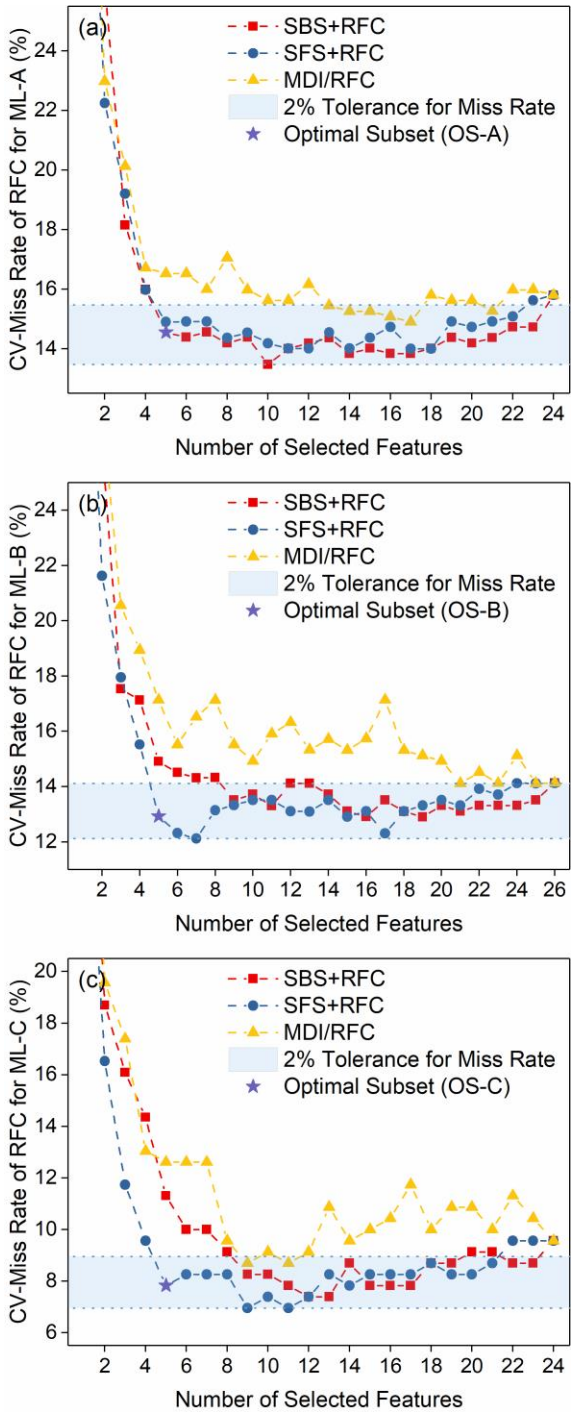

Figure 4. The miss rate of each RFC model with 100 trees versus the feature number for the (a) ML-A, (b) ML-B, and (c) ML-C dataset.

Accordingly, Figures 4(a, b, c) show the miss rate of each RFC model versus feature rank number in the ML-A, ML-B, and ML-C datasets, respectively, where the miss rate is the averaged value of ten miss rates from the ten-fold cross-validation. As expected, when the feature number increases, the miss rate decreases, reaches a minimum and then increases. The validation minimum in the miss rate determines the feature number, which are 10, 7, and 9 corresponding to the SBS+RFC feature set for the ML-A dataset, the SFS+RFC feature set for

the ML-B dataset, and the SFS+RFC feature set for the ML-C dataset, respectively. In addition to showing the determined feature numbers, Figures 4(a, b, c) all indicate the miss rate decreases very slow when the feature number is larger than a critical value, which allows one to further reduce the feature numbers under the cost of acceptable loss in the prediction power. Here, we suggest a tolerance of 2% around the validation minimum of miss rate to balance performance and complexity, which is clearly shown in each of Figures 4(a, b, c). With the 2% tolerance, we select the OS-A, OS-B, and OS-C feature sets for the classifications of the ML-A, ML-B, and ML-C datasets, respectively. Table 3 lists the OS-A, OS-B, and OS-C feature sets, indicating each set contains 5 features. Table 3 indicates that feature H_{mix} appears in all three feature sets, δ_{Cm} appears in both OS-A and OS-B, $\overline{AN}$ appears in both OS-B and OS-C. Thus, the total number of different features is 11, and the 11 features can be used to predict the mechanical properties of CCAs.

Table 3. Finally selected features for ML-A, ML-B, and ML-C datasets.

Dataset	Feature set	Method	Features sorted by the feature rank
ML-A	OS-A	SBS+RFC	$\overline{MR}$, δ_{Tb}, H_{mix}, $\overline{Eea}$, δ_{Cm}
ML-B	OS-B	SFS+RFC	$\overline{\mathrm{VEC}}$, $\overline{AN}$, H_{mix}, δ_K, δ_{Cm}
ML-C	OS-C	SFS+RFC	$\overline{AN}$, δ_{AN}, δ_{XP}, $\overline{K}$, H_{mix}

The OS-A feature set includes the five features of enthalpy of mixing (H_{mix}), mismatch in boiling temperature (δ_{Tb}), mismatch in molar heat capacity (δ_{cm}), average metallic radius ($\overline{MR}$), and average electron affinity ($\overline{Eea}$). The previous studies indicate that a near zero of H_{mix} value leads to the formation of single-phase CCAs, a medium negative H_{mix} promotes the formation of amorphous; otherwise, the multi-phase CCAs exist [26,62,63]. This might be because the Gibbs free energy of mixing is expressed by $G_{mix} = H_{\mathrm{mix}} - S_{\mathrm{mix}} \cdot \overline{T_m}$ and thus the smaller the absolute value of H_{mix} is, the larger the contribution of S_{mix} will be. The boiling temperature and the molar heat capacity may reflect the bond strength, thus, δ_{Tb} and δ_{cm} might be considered as an estimator of the mismatch in metallic radius (δ_{MR}). Zhang et al. [56] found that amorphous phases are formed when δ_{MR} is large, while single-phase CCAs are more like to possess a small δ_{MR}. Fukuhara et al. found that amorphous alloys tend to have more valence

electrons than crystalline alloys [64,65], thus the value of $\overline{MR}$ and $\overline{Eea}$ affects the formation of AM phase.

The OS-B feature set contains enthalpy of mixing (H_{mix}), mismatch in thermal conductivity (δ_K), mismatch in molar heat capacity (δ_{cm}), average valence electron ($\overline{\mathrm{VEC}}$), and average atomic number ($\overline{AN}$). The presence of H_{mix} is in agreement with empirical rules [66,67]. The thermal conductivity of Co, Cr, Fe, and Ni are all between 80~100 W/m/K, while Mn and Cu have significantly different thermal conductivities of 8 and 400 W/m/K, respectively [26]. Thus, a larger δ_K might lead to the formation of solid solutions and a smaller value of δ_{cm} might stabilize solid solutions. Tsai et al. [68] show that the σ phase only exists in the range of $6.88 < \overline{\mathrm{VEC}} < 7.84$ in as-cast Cr- and V- containing CCAs, Leong et al. [69] found that B2 phase presence at $\overline{\mathrm{VEC}} \leq 6.81$ in CoCrFeNi-Al_x CCAs and C14 phase presence at $\overline{\mathrm{VEC}} \leq 7.4$ in CoCrFeNi-Ti_x CCAs, these observations demonstrate that the $\overline{\mathrm{VEC}}$ is another essential feature of the phase formation in CCAs. The $\overline{AN}$ is a coarse estimation of the average number of electrons, too many electrons might destabilize the solid solutions [70].

The OS-C feature set contains enthalpy of mixing (H_{mix}), mismatch in atomic number (δ_{AN}), mismatch in Pauling electronegativity (δ_{XP}), average thermal conductivity ($\overline{K}$), and average atomic number ($\overline{AN}$). The feature of H_{mix} appears in all the three feature sets, thereby indicating that H_{mix} plays an important role in the phase formation ability. The FCC or HCP structure has a packing fraction of 74%, while the BCC has a packing fraction of 68%. Therefore, BCC structures might have larger δ_{MR} (indicating larger δ_{AN}) than FCC or HCP structures [71]. A larger δ_{XP} might promote the segregation behaviors in as-cast CCAs, which makes BCC phase formation possible from the FCC matrix [72]. The phase formation depends on the cooling rate during the cast and therefore $\overline{K}$ is selected to be an important feature. The elements of Al, Cr, Fe, and Mn are BCC stabilizers, while elements of Co, Ni, and Cu are FCC stabilizers in CCAs [71]. Therefore, the feature $\overline{AN}$ plays an important role in the phase classification.

The hyperparameters of RFC models are optimized with the selected features to the values listed in Table 4 by grid search algorithms from the presets [73]. The confusion matrices in Figure 5 (a, b, c) show the detailed cross-validation classification results on the ML-A, ML-B, and ML-C datasets, respectively. The RFC models achieve the correct predictions of 92.10%, 74.85%, and 85.25% to classify the three phases of AM, SP, and MP in the ML-A dataset, 83.04%

and 92.48% to classify the two phases of SS and IM in the ML-B dataset, and 100.0%, 95.83%, 92.65%, and 87.50% to classify the four phases of HCP, BCC, FCC, and MSS in the ML-C dataset, respectively. The results demonstrate that the RFC models are robust and reliable for predicting the phase-formation in CCAs.

Table 4. Hyperparameters in the RFC models.

Dataset	*n_estimators*	*max_features*	*max_depth*
	Preset: [64, 128]	Preset: [1,5]	Preset: None and [5, 10]
ML-A	88	4	None
ML-B	86	1	None
ML-C	92	3	7

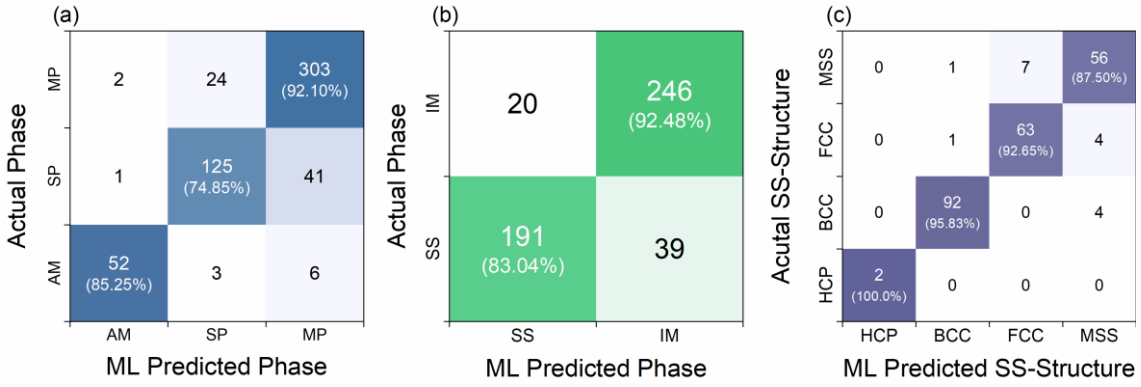

Figure 5. The confusion matrixes of the RFC models on the (a) ML-A, (b) ML-B, and (c) ML-C datasets.

3.2 Prediction of mechanical properties

As mentioned before (see Figure 1), the mechanical properties of CCAs, such as hardness and UTS, are highly dependent on their formed phases. The selected 11 features, listed in Table 3, have significant effects on the phase formation of CCAs and must play considerable roles in the mechanical properties of CCAs. Therefore, the selected 11 features, rather than the originally proposed 30 features, are used here as the initial features in the ML of the hardness and UTS of CCAs. Due to the relatively small feature space, a brute force search approach, best subset selector wrapper with RFR algorithms (BSS+RFR) are conducted to search for the best subset from all possible (2^{11}-1) subsets for the regressions of hardness and UTS.

Figure 6(a) illustrates the regression *NRMSE* in terms of hardness versus feature number obtained from the ten-fold cross-validation, showing that the *NRMSE* reaches the lowest value

of 0.1550 with 6 features selected by BSS+RFR. Figure 7(a) plots the regression *NRMSE* in terms of UTS versus feature number obtained from the ten-fold cross-validation, showing that the *NRMSE* reaches the lowest value of 0.1886 with 5 features selected by BSS+RFR.

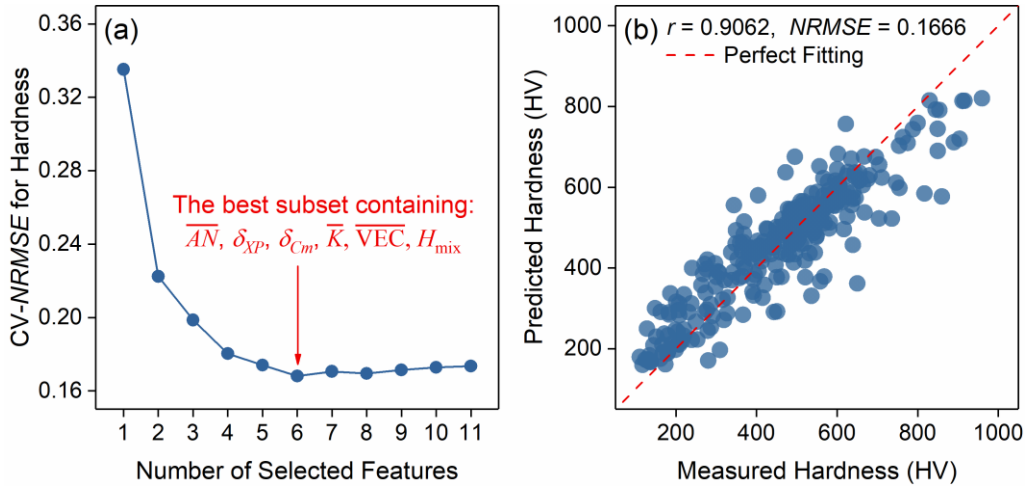

Figure 6. (a) The cross-validated *NRMSE* versus the feature number of each RFR model for hardness prediction, (b) ML-predicted hardness versus the measured values.

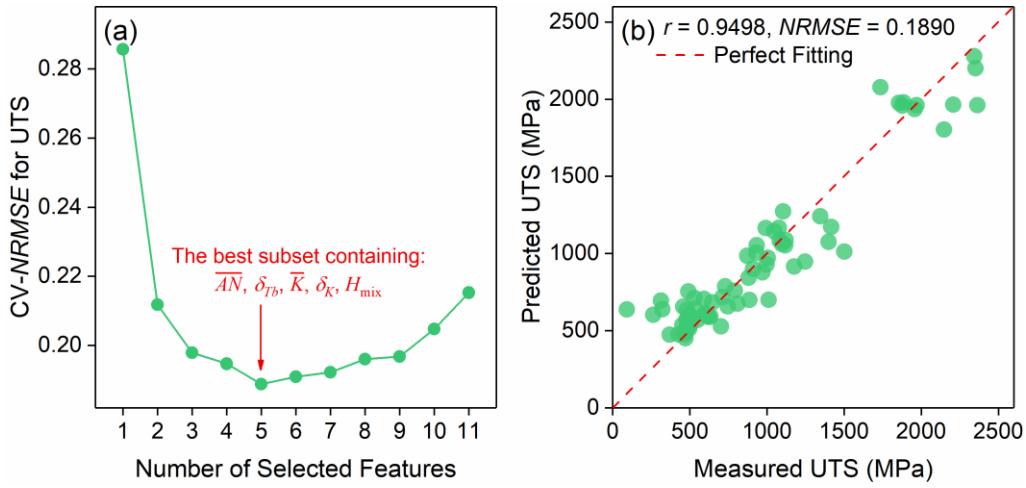

Figure 7. (a) The cross-validated *NRMSE* versus the feature number of each RFR model for UTS prediction, (b) ML-predicted UTS versus the measured values.

Table 5. Hyperparameters in the RFR models.

Dataset	*n_estimators*		*max_features*		*max_depth*		CV-*r*
	preset	result	preset	result	preset	result	
Hardness	[64, 128]	90	[1, 6]	2	None and [5, 10]	None	0.9062
UTS	[64, 128]	74	[1, 5]	1	None and [5, 10]	None	0.9498

The grid search algorithm is then employed here to tune the hyperparameters of RFR models on selected features, and the results are listed in Table 5. Figures 6(b) and 7(b) show the predicted hardness and UTS from the trained RFR models with the selected features against the actual values, respectively, indicating $r = 0.9062$ for hardness and $r = 0.9498$ for UTS.

In addition, the Shapley additive explanation (SHAP) approach is employed here to analyze features, which can explore the contribution of each of features in the trained RFR model to the predictions of hardness and UTS. The SHAP approach is developed based on the game theory that partitions each prediction into individual feature contributions [74]. The SHAP value of the i-th feature is calculated by

$$\varphi_i = \sum_{S \sqsubseteq F \backslash \{i\}} \frac{|S|!\,(|F| - |S| - 1)!}{|F|!} \left[f_{S\cup\{i\}}(x_{S\cup\{i\}}) - f_S(x_S) \right] \tag{10}$$

where F is the set of all features, S is the subset of F, $S \cup \{i\}$ is the union of the subset S and the i-th feature, $f_{S\cup\{i\}}(x_{S\cup\{i\}})$ is the prediction of the model with the i-th feature, and $f_S(x_S)$ is the prediction of the model trained without the i-th feature. Adding up contributions from all features yields the prediction, i.e.,

$$\hat{y} = \hat{y}_0 + \sum_{i=1}^{n} \varphi_i \tag{11}$$

where $\hat{y}$ is the predicted value and $\hat{y}_0$ is the prediction without any features, Equations (10, 11) are applied to every datum, viz., the SHAP value varies with the datum. The mean absolute value of the SHAP values for each feature can be computed here to get its impact on the targeted property. Furthermore, since hardness and UTS are both such properties with positive values that when the SHAP value of a feature is positive, the feature improves the properties; conversely, a feature with a negative SHAP value weakens them.

Figure 8(a) plots and ranks the mean absolute SHAP values of 6 hardness features selected by BSS+RFR, where the mean absolute SHAP values of the three most important features ($\overline{\text{VEC}}$, H_{mix}, δ_{XP}) are much greater than other features. Figures 8 (b-g) plot the SHAP value on every datum of the hardness data, of the six selected features, $\overline{\text{VEC}}$, H_{mix}, δ_{XP}, $\overline{AN}$, δ_{Cm}, and $\overline{K}$ respectively. An extremely important finding is that there exists a critical value to each of the three most important features, which almost sharply separates the SHAP values into positive and negative two regions. The SHAP values are positive when the features $\overline{\text{VEC}} < 7.67$

$H_{\mathrm{mix}} < -9.8\ \mathrm{kJ/mol}$, and $\delta_{XP} > 0.067$, regardless there are some data located in the wrong region in the SHAP value versus δ_{XP} plot. This finding is significant to the design of high hardness CCAs, because it provides the right value regions of the top three features.

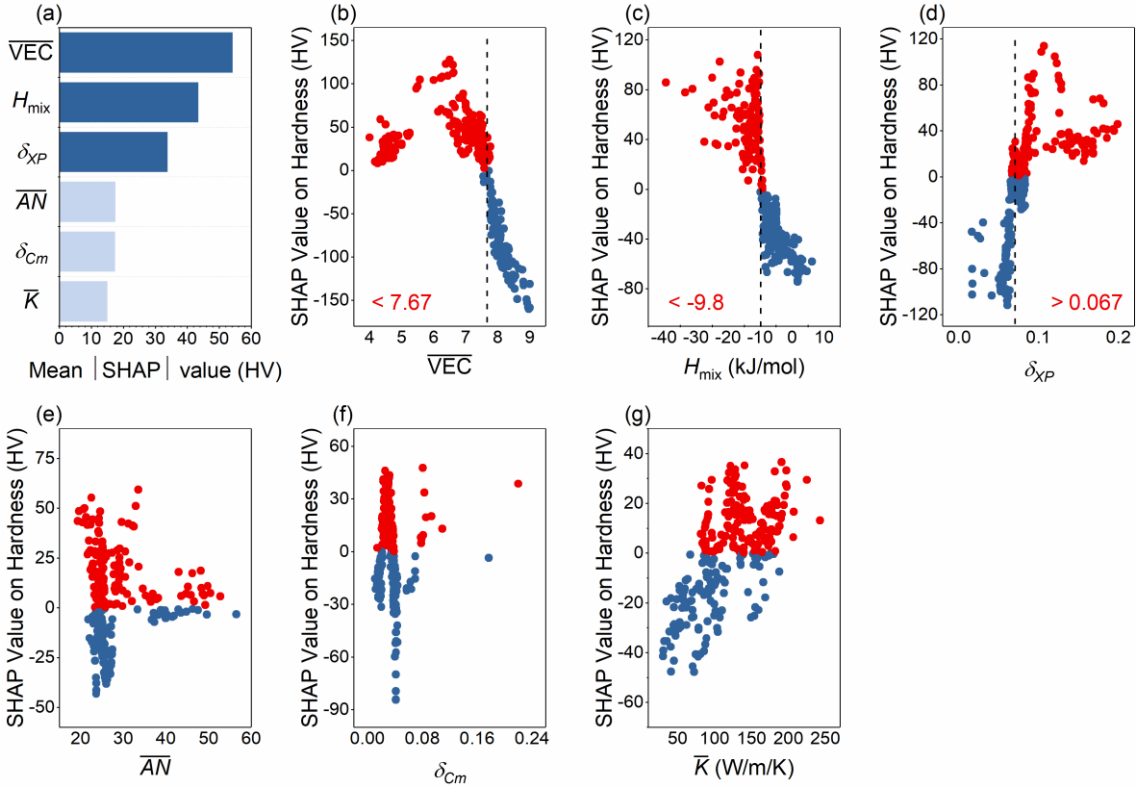

Figure 8. (a) Ranked mean absolute value of SHAP values of the 6 BSS+RFR selected features for hardness. The SHAP values (negative in blue, positive in red) of (b) $\overline{\mathrm{VEC}}$, (c) H_{mix}, (d) δ_{XP}, (e) $\overline{AN}$, (f) δ_{Cm}, and (g) $\overline{K}$ for every one of the data.

The same behavior regarding the separation of positive and negative SHAP values is found in the plots of SHAP value versus UTS feature. Figure 9(a) shows the mean absolute SHAP values of 5 UTS features selected by BSS+RFR and the two most important features of δ_{Tb} and H_{mix} have the mean absolute SHAP value greater than 100 MPa. Figure 9(b-c) show that the SHAP values are positive when $\delta_{Tb} > 0.15$ and $H_{\mathrm{mix}} < -14.6\ \mathrm{kJ/mol}$, regardless there is one datum located in the wrong region in the SHAP value versus H_{mix} plot. If one is going to design high UTS CCAs, one can select elements with the top two features located in the right regions.

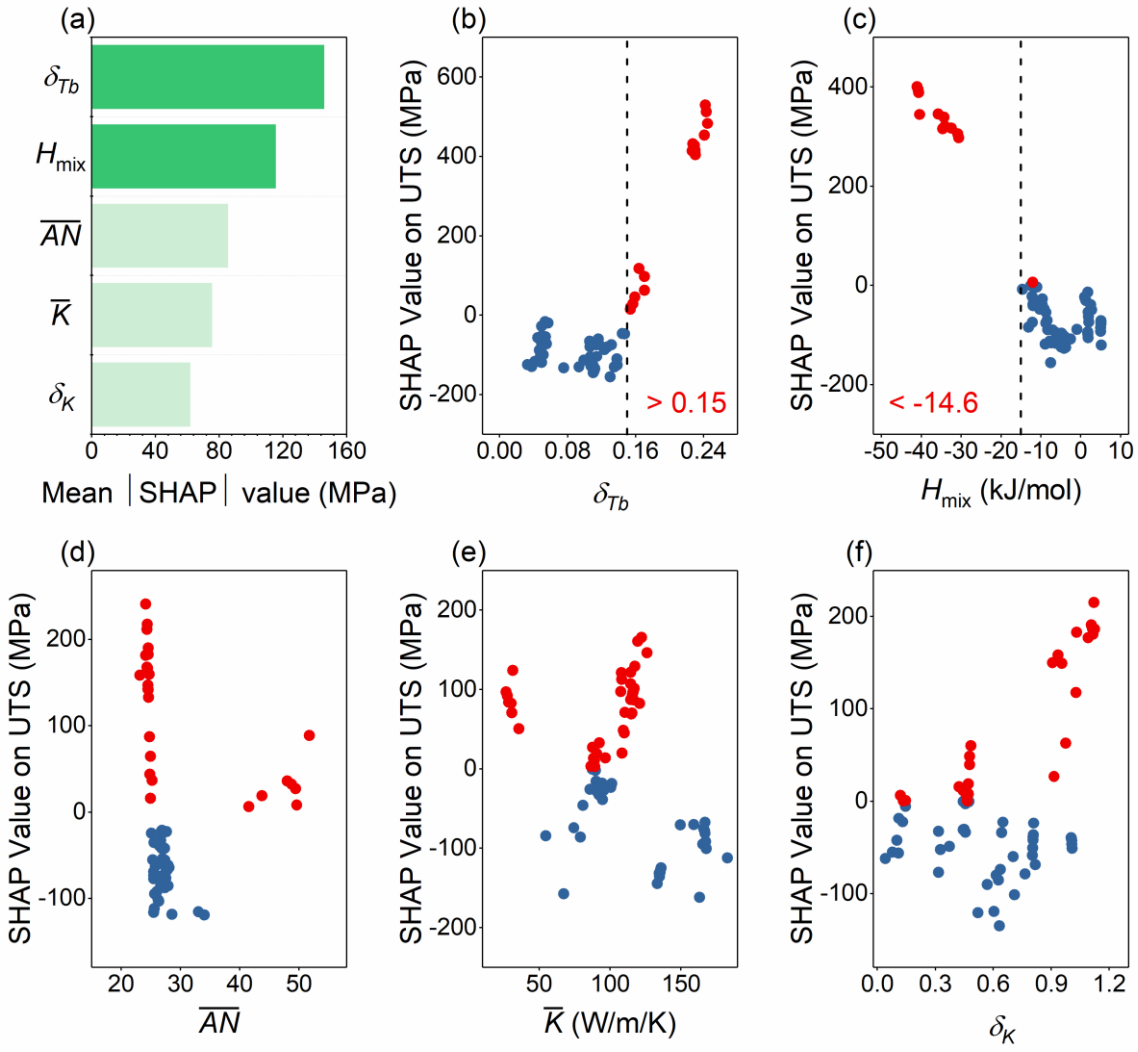

Figure 9. (a) Ranked mean absolute value of SHAP values of the 5 BSS+RFR selected features for UTS. The SHAP values (negative in blue, positive in red) of (b) δ_{Tb}, (c) H_{mix}, (d) $\overline{AN}$, (f) $\overline{K}$, and (g) δ_K for every one of the data.

3.3 Design of high hardness and high UTS CCAs

The SHAP values of these top features provide guidance to the design of novel CCAs with high hardness and high UTS. As an example, we take the CoCrFeNi CCA as the parent CCA to show how to strengthen and harden it, under the guidance of the SHAP values, by adding another element, which leads to equimolar quinary CCAs with each having five elements. These transition elements of Ti, V, Mn, Cu, Zr, Nb, and Hf are selected as candidates. The feature values of $\overline{\mathrm{VEC}}$, H_{mix}, δ_{XP}, and δ_{Tb} in the parent CoCrFeNi CCA are 8.25, -3.75 kJ/mol, 0.0531, and 0.0328, respectively, as shown in Table 6. Simple calculations give the feature

values of $\overline{\mathrm{VEC}}$, H_{mix}, δ_{XP}, and δ_{Tb} in CoCrFeNi-X (X=Ti, V, Mn, Cu, Zr, Nb, or Hf), which are shown in Table 6 also.

Clearly, adding Zr, Nb, or Hf element makes the feature values of $\overline{\mathrm{VEC}}$ and H_{mix} lower than the corresponding critical values and the feature values of δ_{XP}, and δ_{Tb} higher than the corresponding critical values. Then, as expected, the ML predicted hardness and UTS of CoCrFeNi-X (X=Zr, Nb, or Hf) are greatly enhanced, which might be caused by Laves phases. On the other hand, adding V, Mn, or Cu cannot make the feature values of $\overline{\mathrm{VEC}}$ and H_{mix} lower than the corresponding critical values and the feature values of δ_{XP}, and δ_{Tb} larger than the corresponding critical values. Therefore, the ML predicted hardness and UTS of CoCrFeNi-X (X= V, Mn, or Cu) are not improved significantly. In addition, adding Ti makes the feature values of $\overline{\mathrm{VEC}}$ and H_{mix} lower than the corresponding critical values and the feature value of δ_{XP} larger than the corresponding critical value, the ML predicted hardness of CoCrFeNiTi is thus improved significantly, while the predicted UTS is not improved due to a small δ_{Tb} value.

Table 6. The feature values, ML-predicted, and mechanical properties of CoCrFeNi-X (X=Ti, V, Mn, Cu, Zr, Nb, or Hf) CCAs, where mechanical properties and structures in parentheses are measured values.

Alloy	$\overline{\mathrm{VEC}}$	H_{mix}	δ_{XP}	δ_{Tb}	Hardness (HV)	UTS (MPa)	Phases
CoCrFeNi	8.25	-3.75	0.0531	0.0328	173.6 (129.8 [75])	527.3 (480 [76])	SP-FCC (FCC [75])
CoCrFeNiTi	7.4	-16.32	0.0802	0.0623	592.6	655.0	MP-IM
CoCrFeNiV	7.6	-8.96	0.0646	0.0754	377.5	424.1 (311 [39])	MP-IM (FCC+σ [39])
CoCrFeNiMn	8	-4.16	0.0783	0.1101	175.7 (144.0 [77])	495.9 (494 [39])	SP-FCC (FCC [77])
CoCrFeNiCu	8.8	3.2	0.0502	0.0474	152.9	558.3	SP-FCC
CoCrFeNiZr	7.4	-22.72	0.1244	0.1846	616.5	1133.3	MP-IM (BCC+C15 [78])
CoCrFeNiNb	7.6	-14.88	0.0694	0.2191	615.2 (602 [79])	1293.1	MP-IM (FCC+C14 [79])
CoCrFeNiHf	7.4	-19.52	0.1313	0.2047	586.1	1209.0	MP-IM (BCC+C36 [78])

As seen in Table 6, a lower $\overline{\mathrm{VEC}}$ [68,69] promotes the formation of IM phases, such as σ phases or Laves phases, which are harder than solid solutions. Therefore, a lower $\overline{\mathrm{VEC}}$ can harden the CCAs. A smaller mismatch leads to the formation of solid solutions, which are softer

and weaker than IM phases, thus a larger δ_{XP} and δ_{Tb} can harden and strengthen CCAs, respectively. A near zero of H_{mix} value leads to the formation of single-phase solid solutions (SP-FCC for CoCrFeNi, CoCrFeNiMn, and CoCrFeNiCu). Thus, a much negative H_{mix} can harden and strengthen CCAs.

Concluding remarks

The present work illustrates an ML framework to predict the formed phases, the hardness, and the UTS of CCAs. A dataset of 557 samples is constructed, and 30 initial features are proposed. The adopted feature selection method gives the five features of $\overline{MR}$, δ_{Tb}, H_{mix}, $\overline{Eea}$, and δ_{Cm} in the classification of AM, SP, and MP phases, the five features of $\overline{\text{VEC}}$, $\overline{AN}$, H_{mix}, δ_K, and δ_{Cm} in the classification of SS and IM, and the five features of $\overline{AN}$, δ_{AN}, δ_{XP}, $\overline{K}$, and H_{mix} in the classification of mixed solid solutions, pure BCC, FCC, and HCP. All the ML models can classify the formed phases accurately.

The most significant finding in the present ML regressions of hardness and UTS of CCAs is the critical value in each of the four most important features ranked by the absolute SHAP value. The critical feature value separates the SHAP values into positive and negative regions. This means that the feature values in the positive/negative SHAP value region improve/impair the mechanical properties of CCAs, thereby providing a straightforward assessment in the design of high hardness and high UTS CCAs. A demonstration of such a novel design methodology is illustrated in the present work. Since all data collected are as-cast CCAs, the ML suggested high hardness and high UTS CCAs should be fabricated by the cast.

It should be kept in mind that the mathematic basis of ML is probability and statistics, and thus ML predictions depend highly on data and should be understood in the sense of probability. It is a great challenge to develop knowledge from data. Understanding why there exists the critical value in each of the four most important features calls for more deep and comprehensive investigations from both materials science and ML approaches.

Acknowledgments

The work is supported by the National Key R&D Program of China (No. 2018YFB0704404),

the Hong Kong Polytechnic University (internal grant nos. 1-ZE8R and G-YBDH), and the 111 Project of the State Administration of Foreign Experts Affairs and the Ministry of Education, China (grant no. D16002).

Software

All ML approaches are performed on Python. The SBS and SFS algorithms are available in Mlxtend libraries, the SHAP values are calculated by the SHAP library, and other algorithms are available in scikit-learn libraries.

CRediT authorship contribution statement

Jie Xiong: Conceptualization, Investigation, Methodology, Data curation, Manuscript draft.

San-Qiang Shi: Supervision, Manuscript review, Funding acquisition.

Tong-Yi Zhang: Supervision, Methodology, Manuscript review & editing.

Declaration of competing interest

The authors declare that they have no known competing financial interests or personal relationships that could have appeared to influence the work reported in this paper.

References

[1] J.W. Yeh, Ann Chim Sci Des Mater 31 (2006) 633–648.

[2] M.H. Tsai, J.W. Yeh, Mater Res Lett 2 (2014) 107–123.

[3] C. Zhang, M.C. Gao, in: High-Entropy Alloy, Springer International Publishing, Cham, 2016, pp. 399–444.

[4] Z. Li, D. Raabe, JOM 69 (2017) 2099–2106.

[5] O.N. Senkov, D.B. Miracle, K.J. Chaput, J.-P. Couzinie, J Mater Res 33 (2018) 3092–3128.

[6] K. Pan, Y. Yang, S. Wei, H. Wu, Z. Dong, Y. Wu, S. Wang, L. Zhang, J. Lin, X. Mao, J Mater Sci Technol 60 (2021) 113–127.

[7] Y. Wu, F. Zhang, X. Yuan, H. Huang, X. Wen, Y. Wang, H. Wu, X. Liu, H. Wang, S. Jiang,

385 Z. Lu, J Mater Sci Technol 62 (2020) 214–220.
386 [8] B. Cantor, I.T.H.H. Chang, P. Knight, A.J.B.B. Vincent, Mater Sci Eng A 375–377 (2004)
387 213–218.
388 [9] M.C. Gao, D.B. Miracle, D. Maurice, X. Yan, Y. Zhang, J.A. Hawk, J Mater Res 33 (2018)
389 3138–3155.
390 [10] M. Gao, D. Alman, Entropy 15 (2013) 4504–4519.
391 [11] T.T. Zuo, R.B. Li, X.J. Ren, Y. Zhang, J Magn Magn Mater 371 (2014) 60–68.
392 [12] A. Takeuchi, K. Amiya, T. Wada, K. Yubuta, W. Zhang, JOM 66 (2014) 1984–1992.
393 [13] Y.F. Kao, S.K. Chen, J.H. Sheu, J.T. Lin, W.E. Lin, J.W. Yeh, S.J. Lin, T.H. Liou, C.W.
394 Wang, Int J Hydrogen Energy 35 (2010) 9046–9059.
395 [14] N.Y. Yurchenko, N.D. Stepanov, S. V. Zherebtsov, M.A. Tikhonovsky, G.A. Salishchev,
396 Mater Sci Eng A 704 (2017) 82–90.
397 [15] C.M. Lin, H.L. Tsai, Intermetallics 19 (2011) 288–294.
398 [16] X. Yang, S.Y. Chen, J.D. Cotton, Y. Zhang, JOM 66 (2014) 2009–2020.
399 [17] Q.W. Xing, Y. Zhang, Chinese Phys B 26 (2017) 1–9.
400 [18] S. Gorsse, F. Tancret, J Mater Res (2018).
401 [19] W.P. Huhn, M. Widom, JOM (2013).
402 [20] T. ZHANG, Y. HE, J. WANG, S. SUN, Sci Sin Technol 49 (2019) 1148–1158.
403 [21] J. Xiong, T. Zhang, S. Shi, Sci China Technol Sci 63 (2020) 1247–1255.
404 [22] X. Geng, H. Wang, W. Xue, S. Xiang, H. Huang, L. Meng, G. Ma, Comput Mater Sci
405 (2020).
406 [23] Y.T. Sun, H.Y. Bai, M.Z. Li, W.H. Wang, J Phys Chem Lett 8 (2017) 3434–3439.
407 [24] F. Ren, L. Ward, T. Williams, K.J. Laws, C. Wolverton, J. Hattrick-Simpers, A. Mehta,
408 Sci Adv 4 (2018).
409 [25] J. Xiong, T.Y. Zhang, S.Q. Shi, Mrs Commun 9 (2019) 576–585.
410 [26] J. Xiong, S.Q. Shi, T.Y. Zhang, Mater Des (2020).
411 [27] L. Ward, S.C. O'Keeffe, J. Stevick, G.R. Jelbert, M. Aykol, C. Wolverton, Acta Mater
412 159 (2018) 102–111.
413 [28] D.Z. Xue, D.Q. Xue, R.H. Yuan, Y.M. Zhou, P. V Balachandran, X.D. Ding, J. Sun, T.
414 Lookman, Acta Mater 125 (2017) 532–541.

[29] C. Wen, Y. Zhang, C.X. Wang, D.Z. Xue, Y. Bai, S. Antonov, L.H. Dai, T. Lookman, Y.J. Su, Acta Mater 170 (2019) 109–117.
[30] N. Islam, W. Huang, H.L. Zhuang, Comput Mater Sci (2018).
[31] W. Huang, P. Martin, H.L. Zhuang, Acta Mater (2019).
[32] U. Bhandari, M.R. Rafi, C. Zhang, S. Yang, Mater Today Commun (2020) 101871.
[33] D.B. Miracle, Jom 69 (2017) 2130–2136.
[34] J.P. Couzinié, O.N. Senkov, D.B. Miracle, G. Dirras, Data Br (2018).
[35] S. Gorsse, M.H. Nguyen, O.N. Senkov, D.B. Miracle, Data Br (2018).
[36] M.H. Tsai, J.W. Yeh, Mater Res Lett (2014).
[37] W.H. Wang, Prog Mater Sci 57 (2012) 487–656.
[38] A. V. Kuznetsov, D.G. Shaysultanov, N.D. Stepanov, G.A. Salishchev, O.N. Senkov, Mater Sci Eng A 533 (2012) 107–118.
[39] J.Y. He, W.H. Liu, H. Wang, Y. Wu, X.J. Liu, T.G. Nieh, Z.P. Lu, Acta Mater 62 (2014) 105–113.
[40] Y. Ma, Q. Wang, B.B. Jiang, C.L. Li, J.M. Hao, X.N. Li, C. Dong, T.G. Nieh, Acta Mater (2018).
[41] H. Huang, Y. Wu, J. He, H. Wang, X. Liu, K. An, W. Wu, Z. Lu, Adv Mater 29 (2017) 1–7.
[42] A. Asabre, A. Kostka, O. Stryzhyboroda, J. Pfetzing-Micklich, U. Hecht, G. Laplanche, Mater Des 184 (2019) 108201.
[43] G. Dirras, L. Lilensten, P. Djemia, M. Laurent-Brocq, D. Tingaud, J.P. Couzinié, L. Perrière, T. Chauveau, I. Guillot, Mater Sci Eng A (2016).
[44] L. Liu, J.B. Zhu, L. Li, J.C. Li, Q. Jiang, Mater Des 44 (2013) 223–227.
[45] L. Liu, J.B. Zhu, C. Zhang, J.C. Li, Q. Jiang, Mater Sci Eng A 548 (2012) 64–68.
[46] C. Ng, S. Guo, J. Luan, Q. Wang, J. Lu, S. Shi, C.T. Liu, J Alloys Compd (2014).
[47] G.A. Salishchev, M.A. Tikhonovsky, D.G. Shaysultanov, N.D. Stepanov, A. V. Kuznetsov, I. V. Kolodiy, A.S. Tortika, O.N. Senkov, J Alloys Compd (2014).
[48] C.J. Tong, Y.L. Chen, S.K. Chen, J.W. Yeh, T.T. Shun, C.H. Tsau, S.J. Lin, S.Y. Chang, Metall Mater Trans A Phys Metall Mater Sci 36 (2005) 881–893.
[49] W.H. Liu, J.Y. He, H.L. Huang, H. Wang, Z.P. Lu, C.T. Liu, Intermetallics 60 (2015) 1–

8.

[50] Y.D. Wu, Y.H. Cai, T. Wang, J.J. Si, J. Zhu, Y.D. Wang, X.D. Hui, Mater Lett 130 (2014) 277–280.

[51] Y. Deng, C.C. Tasan, K.G. Pradeep, H. Springer, A. Kostka, D. Raabe, Acta Mater 94 (2015) 124–133.

[52] L. Zhang, Y. Zhou, X. Jin, X. Du, B. Li, Scr Mater (2018).

[53] Z.Y. Rao, X. Wang, J. Zhu, X.H. Chen, L. Wang, J.J. Si, Y.D. Wu, X.D. Hui, Intermetallics 77 (2016) 23–33.

[54] Y. Lu, X. Gao, L. Jiang, Z. Chen, T. Wang, J. Jie, H. Kang, Y. Zhang, S. Guo, H. Ruan, Y. Zhao, Z. Cao, T. Li, Acta Mater (2017).

[55] X. Jin, Y. Zhou, L. Zhang, X. Du, B. Li, Mater Lett (2018).

[56] Y. Zhang, Y.J. Zhou, J.P. Lin, G.L. Chen, P.K. Liaw, Adv Eng Mater 10 (2008) 534–538.

[57] Y. Zhang, T.T. Zuo, Z. Tang, M.C. Gao, K.A. Dahmen, P.K. Liaw, Z.P. Lu, Prog Mater Sci (2014).

[58] J.W. Yeh, Y.L. Chen, S.J. Lin, S.K. Chen, Mater Sci Forum (2007).

[59] L. Breiman, Mach Learn (2001).

[60] Q. Hu, S. Guo, J.M. Wang, Y.H. Yan, S.S. Chen, D.P. Lu, K.M. Liu, J.Z. Zou, X.R. Zeng, Sci Rep (2017).

[61] Y.F. Ye, Q. Wang, J. Lu, C.T. Liu, Y. Yang, Mater Today (2016).

[62] Y. Zhang, Y.J. Zhou, Mater Sci Forum (2007).

[63] R. Kozak, A. Sologubenko, W. Steurer, Zeitschrift Fur Krist (2015).

[64] M. Fukuhara, M. Takahashi, Y. Kawazoe, A. Inoue, J Alloys Compd (2009).

[65] Z. Zhou, Y. Zhou, Q. He, Z. Ding, F. Li, Y. Yang, Npj Comput Mater (2019).

[66] Y. Zhang, Y.J. Zhou, J.P. Lin, G.L. Chen, P.K. Liaw, Adv Eng Mater 10 (2008) 534–538.

[67] S. Guo, C.T. Liu, Prog Nat Sci Mater Int 21 (2011) 433–446.

[68] M.H. Tsai, K.Y. Tsai, C.W. Tsai, C. Lee, C.C. Juan, J.W. Yeh, Mater Res Lett 1 (2013) 207–212.

[69] Z. Leong, J.S. Wróbel, S.L. Dudarev, R. Goodall, I. Todd, D. Nguyen-Manh, Sci Rep (2017).

[70] Y. Zhang, C. Wen, C. Wang, S. Antonov, D. Xue, Y. Bai, Y. Su, Acta Mater (2020).

[71] S.A. Kube, S. Sohn, D. Uhl, A. Datye, A. Mehta, J. Schroers, Acta Mater (2019).

[72] Z.S. Nong, J.C. Zhu, Y. Cao, X.W. Yang, Z.H. Lai, Y. Liu, Mater Sci Technol (United Kingdom) (2014).

[73] T.M. Oshiro, P.S. Perez, J.A. Baranauskas, in: Lect Notes Comput Sci (Including Subser Lect Notes Artif Intell Lect Notes Bioinformatics), 2012.

[74] S.M. Lundberg, S.I. Lee, in: Adv Neural Inf Process Syst, 2017.

[75] W.R.W.L. Wang, W.R.W.L. Wang, S.C. Wang, Y.C. Tsai, C.H. Lai, J.W. Yeh, Intermetallics 26 (2012) 44–51.

[76] W.H. Liu, Z.P. Lu, J.Y. He, J.H. Luan, Z.J. Wang, B. Liu, Y. Liu, M.W. Chen, C.T. Liu, Acta Mater (2016).

[77] N.D. Stepanov, D.G. Shaysultanov, G.A. Salishchev, M.A. Tikhonovsky, E.E. Oleynik, A.S. Tortika, O.N. Senkov, J Alloys Compd 628 (2015) 170–185.

[78] M.H. Tsai, A.C. Fan, H.A. Wang, J Alloys Compd 695 (2017) 1479–1487.

[79] H. Jiang, L. Jiang, D. Qiao, Y. Lu, T. Wang, Z. Cao, T. Li, J Mater Sci Technol 33 (2017) 712–717.